

## Quantum Cascade Surface-Emitting Photonic Crystal Laser

Raffaele Colombelli,<sup>1,5\*</sup> Kartik Srinivasan,<sup>2</sup> Mariano Troccoli,<sup>3</sup>  
Oskar Painter,<sup>2</sup> Claire F. Gmachl,<sup>1,6</sup> Donald M. Tennant,<sup>1,4</sup>  
A. Michael Sergent,<sup>1</sup> Deborah L. Sivco,<sup>1</sup> Alfred Y. Cho,<sup>1</sup>  
Federico Capasso<sup>3</sup>

We combine photonic and electronic band structure engineering to create a surface-emitting quantum cascade microcavity laser. A high-index contrast two-dimensional photonic crystal is used to form a micro-resonator that simultaneously provides feedback for laser action and diffracts light vertically from the surface of the semiconductor surface. A top metallic contact allows electrical current injection and provides vertical optical confinement through a bound surface plasmon wave. The miniaturization and tailorable emission properties of this design are potentially important for sensing applications, while electrical pumping can allow new studies of photonic crystal and surface plasmon structures in nonlinear and near-field optics.

Quantum Cascade (QC) lasers have established themselves as the leading tunable coherent semiconductor source in the mid- and far-infrared (IR) ranges of the electromagnetic spectrum (1–3). Their uniqueness stems from the use of an intraband (and hence unipolar) optical transition between quantized conduction band states (subbands) of a suitably designed multi-quantum well structure. However, due to the transverse magnetic (TM) polarization of intersubband transitions, QC lasers are intrinsically only in-plane emitters. The electric field vector is perpendicular to the semiconductor layers, and surface emission, desirable for several applications, cannot be easily achieved.

We have developed a micro-resonator for QC lasers that provides in-plane feedback and vertical extraction of the laser light. Though previous attempts to develop vertically emitting QC lasers used second-order Bragg gratings superimposed on conventional edge-emitting QC lasers (4–6), they did not address the large size of the devices. As a result of using a deeply

etched two-dimensional (2D) photonic crystal (PC) structure (7), the dimensions of our micro-resonators are greatly scaled down in comparison to standard QC technology, thus opening the way for the miniaturization and on-chip integration of QC lasers for applications involving the use of multiwavelength 2D laser arrays for spectroscopy, gas-sensing, and imaging.

PC-based QC lasers also represent an ideal system to conduct research on photonic bandgap structures. Compared with shorter-wavelength lasers, the smaller ratio between the scale of etch-induced surface roughness and the operating wavelength can considerably reduce optical scattering. Leakage currents due to surface recombination, usually substantially increased by the etching of the semiconductor material, are not present because QC lasers are unipolar devices. This is in contrast with diode lasers, where surface recombination is a serious obstacle to their use in conjunction with PC technology. Finally, the majority of PC micro-resonator laser work thus far has used optical pumping (8). The demonstration of an electrically pumped, small-area PC laser in a nonundercut waveguide geometry is an important step in the development of PC microcavity lasers for practical applications.

Photonic crystals are materials where a spatially periodic modulation of the dielectric constant affects the properties of photons in a manner analogous to the influence of a semiconductor crystal lattice on the properties of electrons (9). Planar PC devices, using a 2D photonic lattice with a conventional slab verti-

cal waveguide, have been an appealing device architecture due to the maturity of planar fabrication methods (10). Two-dimensional PC slab waveguide lasers can be divided in two families: defect mode and band-edge mode lasers. The former operate at frequencies inside the bandgap by incorporating an intentionally introduced defect in the lattice that supports highly localized resonator modes (8). Band-edge mode lasers, in contrast, operate in regions of energy-momentum space with a high photonic density of states (i.e., small group velocity), as a result of the distributed feedback of the lattice (11). To date, defect mode lasers with wavelength-scale cavities have been demonstrated in optically pumped configurations only (8, 12). But band-edge lasers typically are broad-area devices using a relatively shallow etch (weak grating) in a nonmembrane geometry (4–6, 11).

In our PC QC lasers, an etched pattern penetrates through the laser active region, deep into the bottom waveguide cladding. This etch produces the same 2D PC pattern in the lower refractive index bottom cladding as in the waveguide core, allowing for efficient vertical confinement of the guided mode (13). This design reduces the diffraction of radiation into the substrate, while providing a high-index contrast semiconductor-air 2D grating for strong in-plane feedback. As a result, our devices use only 10 periods of the photonic lattice (less than eight wavelengths in diameter), hence, their classification as “microcavity” lasers.

We approximate this planar system as 2D with a refractive index  $n_{\text{eff}}$  given by the effective index of the fundamental vertical waveguide mode (14). The PC is a hexagonal etched array of air holes, chosen not for its frequency bandgaps (in two dimensions, this lattice does not have a complete bandgap for TM-polarized light), but because of its connected nature, a feature necessary for electrical injection. However, the absence of a full 2D bandgap does not prevent the formation of strongly dispersive flat-bands for creating low-loss band-edge states or low-loss localized defect states (15). The main criterion is that the PC provides high-index contrast so that strong optical feedback can be obtained over several lattice periods, setting the scale of the devices.

The calculated in-plane band structure for TM-polarized light (Fig. 1A) was obtained using the plane wave expansion method (16) with  $n_{\text{eff}} = 3.35$  and hole radius ( $r$ ) to lattice spacing ( $a$ ) ratio of  $r/a = 0.30$ . Mixing of forward and backward propagating plane-waves at high-symmetry points of the PC reciprocal lattice results in regions with flat dispersion. In these flat-band regions, low-loss resonant modes can be localized in finite

<sup>1</sup>Bell Laboratories, Lucent Technologies, Murray Hill, NJ 07974, USA. <sup>2</sup>Department of Applied Physics, California Institute of Technology, Pasadena, CA 91125, USA. <sup>3</sup>Division of Engineering and Applied Sciences, Harvard University, Cambridge, MA 02138, USA. <sup>4</sup>New Jersey Nanotechnology Consortium, Murray Hill, NJ 07974, USA. <sup>5</sup>Institut d'Electronique Fondamentale, Bât. 220, Université Paris-Sud, 91405 Orsay, France. <sup>6</sup>Department of Electrical Engineering, Princeton University, Princeton, NJ 08544, USA.

\*To whom correspondence should be addressed. E-mail: colombel@ief.u-psud.fr

lattice structures (such as our cavities) due to the reduction in group velocity over an extended region of wavevector space. Especially important to this work are the three frequency regions highlighted in dark gray in Fig. 1A, which surround the flat-band regions in the frequency range close to the second-order Bragg condition (17). To overlap these band-edge resonances with the QC material gain spectrum ( $\lambda \sim 8 \mu\text{m}$ ), the band structure indicates that  $a$  should be between 2.85 and 3.6  $\mu\text{m}$  for a hexagonal lattice with  $r/a = 0.30$  [see supporting online material (SOM) Text].

Vertical optical confinement is determined by the semiconductor and metal layers comprising the QC laser structure (Fig. 1C). The QC active material used is based on a three-well vertical transition design ( $\lambda \approx 8 \mu\text{m}$ ) (18) and is grown by molecular beam epitaxy on a low-doped InP substrate. A key element of our design is the use of a surface-plasmon waveguide for vertical confinement (19). This waveguide exhibits an electric field intensity maximum at the top semiconductor-metal interface. Particularly relevant to this work is the thinner epitaxial material ( $\approx 2.4 \mu\text{m}$  compared with  $\approx 5.2 \mu\text{m}$  for a standard waveguide) and the absence of AlInAs cladding layers. Both of these characteristics dramatically ease the etching process (Fig. 1D) (20), which must penetrate into the bottom InP cladding to suppress radiation into the substrate (13).

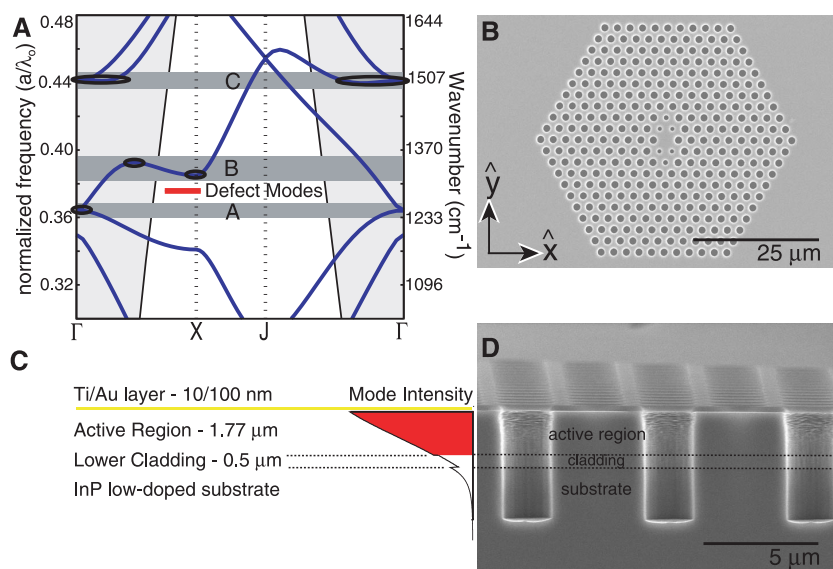
Two-dimensional arrays of devices (fig. S1A) were fabricated with the values of  $a$  and  $r$  systematically varied from device to device ( $2.69 \mu\text{m} < a < 3.00 \mu\text{m}$ ;  $0.28 < r/a < 0.32$ ), allowing the PC modes to be tuned through a range of frequencies encompassing the QC gain peak (21). Two types of cavities were fabricated: one with a central defect (Fig. 1B), and another one with no central defect (a control sample). Electroluminescence (EL) measurements were performed at a temperature of 10 K and light was collected vertically from the top surface of the devices.

Figure 2A (black dashed line) shows that when the PC resonances do not overlap the gain spectrum (for detuned  $r$  or  $a$ ), the emission is near-Lorentzian with a full-width at half-maximum (FWHM) of  $\sim 100 \text{ cm}^{-1}$ . No line-narrowing (indicative of gain) is observed even at high injection currents. For values of  $a$  and  $r$  where the PC resonances overlap with the gain spectrum, three emission peaks (labeled A, B, and C in correspondence with the frequency regions of the band structure in Fig. 1A) emerge on top of the broad EL spectrum (Fig. 2A, red line). The spectral position of these peaks can be tuned as a function of  $a$  and  $r$  (Fig. 2B), confirming that they are related to Bragg scattering in the PC microcavity. In addition, little difference is seen between the emission spectra of cavi-

ties with and without a central defect, ruling out the involvement of highly localized defect states.

To better understand the results, we performed 2D finite-difference time-domain (FDTD) simulations (22) of the finite cavity structure (Fig. 2A, blue line). It shows the presence of three distinct peaks in the

frequency spectrum, in accordance with experiment and the three sets of flat-band regions predicted from band structure calculations. The simulations show that the C peak resonances display a strong field overlap with the air holes, whereas the A and B peaks resonances are confined to semiconductor regions. As a result, we expect the C



**Fig. 1.** (A) Calculated 2D in-plane TM band structure. The flat-band regions (A, B, and C) are indicated by dark gray horizontal bands. For devices with a central defect, the position of the highly localized defect modes is indicated by the thick red line. (B) Top-view scanning electron microscope (SEM) image of an etched device with a central defect (before metal deposition). (C) Layer structure of the device and intensity profile of the surface plasmon mode. (D) Cross-section SEM of a portion of a PC QC device, showing the high surface quality of the etched holes and their depth ( $\sim 4.8 \mu\text{m}$ ).

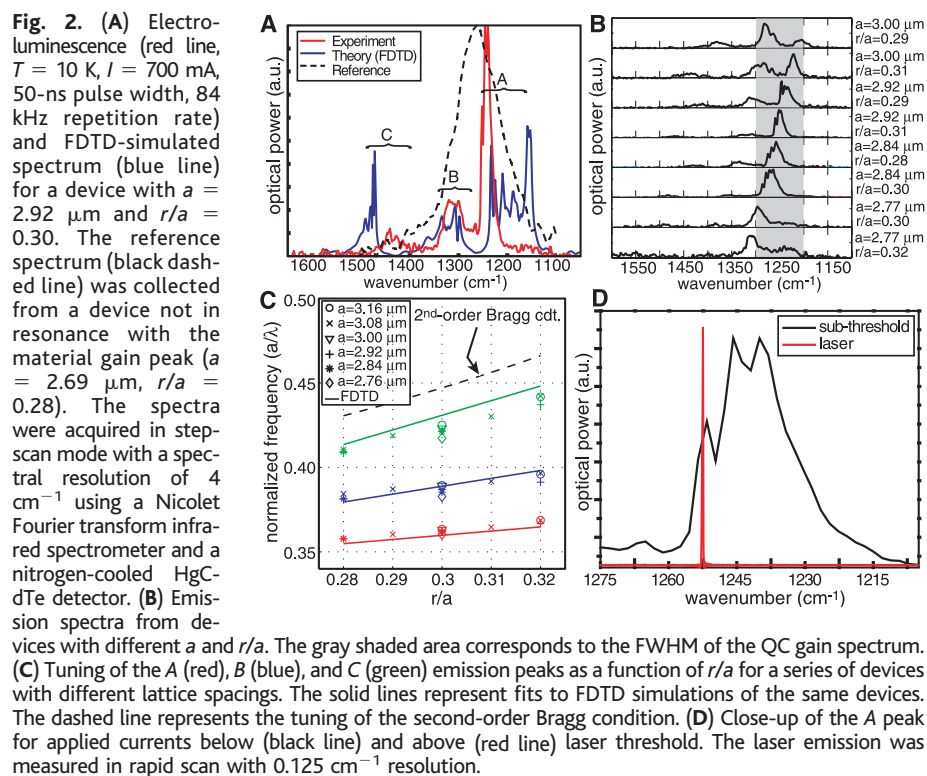


**Fig. 2.** (A) Electroluminescence (red line,  $T = 10 \text{ K}$ ,  $I = 700 \text{ mA}$ , 50-ns pulse width, 84 kHz repetition rate) and FDTD-simulated spectrum (blue line) for a device with  $a = 2.92 \mu\text{m}$  and  $r/a = 0.30$ . The reference spectrum (black dashed line) was collected from a device not in resonance with the material gain peak ( $a = 2.69 \mu\text{m}$ ,  $r/a = 0.28$ ). The spectra were acquired in step-scan mode with a spectral resolution of  $4 \text{ cm}^{-1}$  using a Nicolet Fourier transform infrared spectrometer and a nitrogen-cooled HgCdTe detector. (B) Emission spectra from devices with different  $a$  and  $r/a$ . The gray shaded area corresponds to the FWHM of the QC gain spectrum. (C) Tuning of the A (red), B (blue), and C (green) emission peaks as a function of  $r/a$  for a series of devices with different lattice spacings. The solid lines represent fits to FDTD simulations of the same devices. The dashed line represents the tuning of the second-order Bragg condition. (D) Close-up of the A peak for applied currents below (black line) and above (red line) laser threshold. The laser emission was measured in rapid scan with  $0.125 \text{ cm}^{-1}$  resolution.

## REPORTS

peak to tune more strongly with  $r$  than peaks  $A$  and  $B$ . This prediction is confirmed by both experimental and FDTD results (Fig. 2C). The identification of the highest wavenumber set of resonances in the experimental plot of Fig. 2A as the  $C$  peak provides a reference point from which the  $A$  and  $B$  peaks can then be identified.

Figure 2D (black line) shows a close-up 10 K sub-threshold EL spectrum of the  $A$  peak, revealing that it is composed of three narrower resonances. Such behavior is common to all the measured devices and is in agreement with FDTD simulations (22). Laser emission (Fig. 2D, red line) always starts from the highest wavenumber resonant mode within the  $A$  peak. The current-voltage ( $I$ - $V$ ) characteristic of a typical device (Fig. 3A) shows that the device fabrication was successful, and the large sidewall surface of the holes and deposited metal do not contribute to the leakage cur-

rent. In contrast, the somewhat soft turn-on of the  $I$ - $V$  is probably due to poor current confinement, because no mesa was etched around the devices. The absence of a mesa makes it difficult to accurately estimate the current density at threshold, because the area across which the injected current is spread is unknown. Nevertheless, we estimate a threshold current density of 9 to 10 kA/cm<sup>2</sup> by taking into account a factor of  $\sim 2$  for the current spreading (23). This value should be compared with a threshold of  $\sim 5$  kA/cm<sup>2</sup> obtained from the same QC material processed into conventional mesa stripes. Etching a mesa around the PC may reduce the threshold current density; however, for this first demonstration, its absence is a key feature because it rules out other feedback mechanisms (such as Fabry-Perot-like reflections) and confirms that the PC itself is acting as a microcavity. The majority of the devices exhibit single mode

laser emission in pulsed mode (Fig. 3B, inset). The output wavelength could also be accurately tuned by selecting, from the same semiconductor chip (fig. S1A), devices with different values for  $a$  or  $r$  (Fig. 3B).

The unique identification of the lasing mode was made by comparing far-field emission and polarization measurements with full three-dimensional FDTD simulations (22) (SOM Text). Figure 4, A and B, shows the polarized spatial distributions of the vertically emitted intensity for a typical lasing device, obtained with a micro-bolometer camera, for electric field polarization along the  $[\hat{x}]$  and  $[\hat{y}]$  axes, respectively. The nodal lines along these axes uniquely determine its symmetry classification (labeled  $B_1$  according to group theory notation), consistent with FDTD simulations of the highest frequency (wavenumber) resonant mode of the  $A$  peak (Fig. 2D). Furthermore, calculations of the polarized vertically emitted radiation field (Fig. 4, C and D) are found to be in striking correspondence with the micro-bolometer camera images. As described in the SOM Text, far-field measurements of the laser emission were also performed and are in good agreement with simulation results.

Our PC microcavity lasers combine the electronic bandgap engineering exploited in QC lasers and the optical dispersion engineering of photonic crystals. The result is a photonic crystal injection laser that may open new horizons in device design and application in the mid- to far-IR ranges of the electromagnetic spectrum. Although this is interesting as a proof of concept, there remain significant engineering issues to address in these initial devices to achieve device performance (laser threshold, operation temperature) comparable to standard QC lasers. Second-generation devices will target the problems of current spreading and unwanted metal in the etched holes. Current spreading can be limited by reducing the gap between the  $\text{Si}_x\text{N}_y$  isolation window and the PC lattice and through electrical isolation by ion implantation or mesas. Metal deposition in the etched holes can be avoided by depositing the top metal contact before etching the semiconductor layers. Operation at longer wavelengths will reduce the optical losses in the surface plasmon layer (which, as previously mentioned, limits standard stripe lasers to threshold current densities of a few kA/cm<sup>2</sup>), or alternately, a standard (non-surface plasmon) waveguide may be used. In addition to QC device applications, the control afforded by the electrical injection in these lasers will enable additional flexibility in the study of photonic crystal structures and surface plasmon-mediated optical phenomena, with potential applications in quantum optics and in new lasers based on nonlinear photonic crystals.

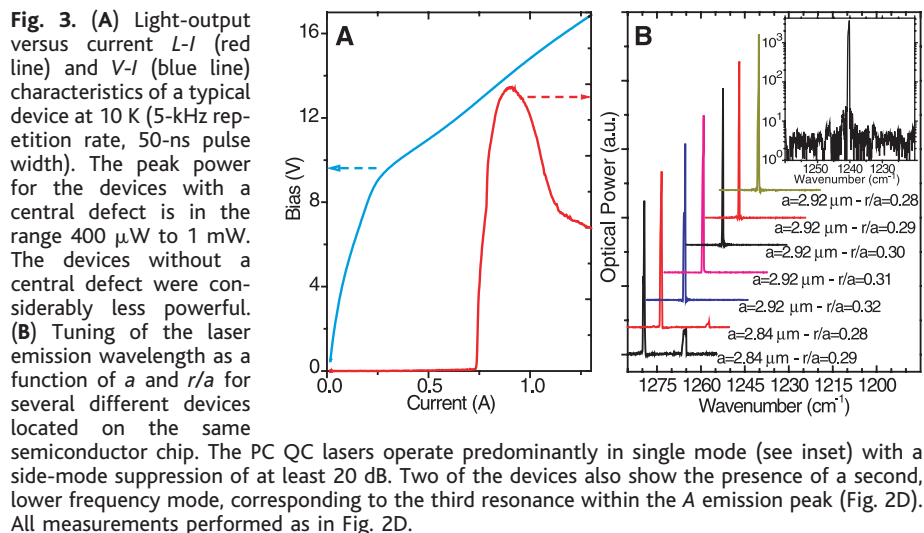


**Fig. 3.** (A) Light-output versus current  $L$ - $I$  (red line) and  $V$ - $I$  (blue line) characteristics of a typical device at 10 K (5-kHz repetition rate, 50-ns pulse width). The peak power for the devices with a central defect is in the range 400  $\mu\text{W}$  to 1 mW. The devices without a central defect were considerably less powerful. (B) Tuning of the laser emission wavelength as a function of  $a$  and  $r/a$  for several different devices located on the same semiconductor chip. The PC QC lasers operate predominantly in single mode (see inset) with a side-mode suppression of at least 20 dB. Two of the devices also show the presence of a second, lower frequency mode, corresponding to the third resonance within the  $A$  emission peak (Fig. 2D). All measurements performed as in Fig. 2D.

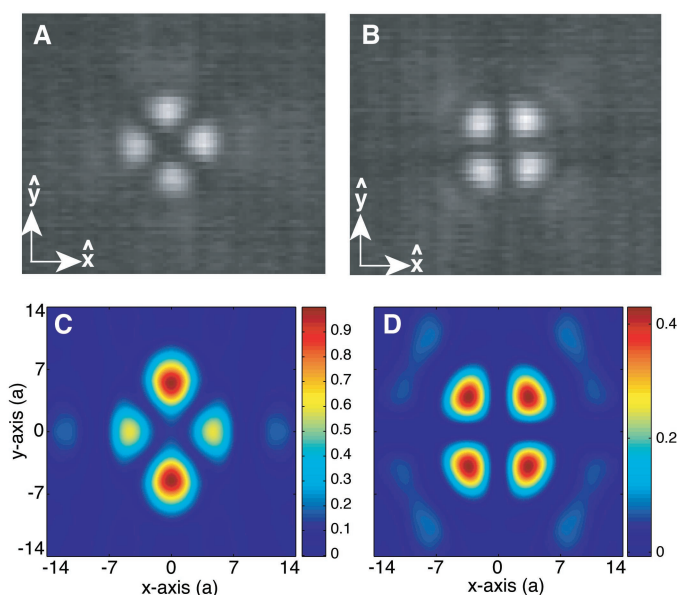


**Fig. 4.** Polarized emission pattern (taken in a plane close to the near field of the PC cavity surface) of a typical lasing device (40-ns pulse width, 100-kHz repetition rate) for a polarization of the electric field along the (A)  $[\hat{x}]$  axis and (B)  $[\hat{y}]$  axis of the cavity. FDTD calculated (C)  $[\hat{x}]$ -polarized and (D)  $[\hat{y}]$ -polarized vertical emission pattern at a few wavelengths above the surface of a nondefect PC cavity.

## References and Notes

1. F. Capasso *et al.*, *IEEE J. Quantum Elect.* **38**, 511 (2002).
2. R. Kohler *et al.*, *Nature* **417**, 156 (2002).
3. M. Beck *et al.*, *Science* **295**, 301 (2002).
4. D. Hofstetter, J. Faist, M. Beck, U. Oesterle, *Appl. Phys. Lett.* **75**, 3769 (1999).
5. W. Schrenk *et al.*, *Appl. Phys. Lett.* **77**, 2086 (2000).
6. I. Vurgaftman, J. R. Meyer, *IEEE J. Quantum Elect.* **39**, 689 (2003).
7. J. D. Joannopoulos, R. D. Meade, J. N. Winn, *Photonic Crystals* (Princeton Univ. Press, Princeton, New Jersey, 1995).
8. O. Painter *et al.*, *Science* **284**, 1819 (1999).
9. J. D. Joannopoulos, P. R. Villeneuve, S. H. Fan, *Nature* **386**, 143 (1997).
10. A. Scherer, J. L. Jewell, J. P. Harbison, *Opt. Photonics News* **2**, 9 (1991).
11. M. Imada *et al.*, *Appl. Phys. Lett.* **75**, 316 (1999).
12. H. Park *et al.*, *Appl. Phys. Lett.* **79**, 3032 (2001).
13. B. D'Urso *et al.*, *J. Opt. Soc. Am. B* **15**, 1155 (1998).
14. O. Painter, J. Vuckovic, A. Scherer, *J. Opt. Soc. Am. B* **16**, 275 (1999).
15. K. Srinivasan, P. E. Barclay, M. Borselli, O. Painter, in press (available at <http://arxiv.org/abs/quant-ph/0309190>).
16. K. Sakoda, *J. Appl. Phys.* **84**, 1210 (1998).
17. Close to the second-order Bragg condition, light can radiate into the air for surface emission as coupling occurs to plane waves with near-zero in-plane momentum. These are the components which lie above the air-light cone (light gray region of Fig. 1A) and can radiate vertically.
18. C. Gmachl *et al.*, *Appl. Phys. Lett.* **72**, 3130 (1998).
19. C. Sirtori *et al.*, *Opt. Lett.* **23**, 1366 (1998).
20. R. Colombelli *et al.*, in preparation.
21. Materials and methods are available as supporting material on *Science* Online.
22. K. Srinivasan *et al.*, in preparation.
23. A. Straub *et al.*, unpublished data.
24. This work was partly supported by Defense Advanced Research Projects Agency (DARPA/ARO) under contract number DAAD19-00-C-0096. We acknowledge useful discussions and help from K. Steeples, M. L. Peabody, A. Straub, K. Baldwin, A. Erbe, and R. Paiella. We thank R. Martini for lending the micro-bolometer camera. K. S. thanks the Hertz Foundation for financial support.

## Supporting Online Material

[www.sciencemag.org/cgi/content/full/1090561/DC1](http://www.sciencemag.org/cgi/content/full/1090561/DC1)  
Materials and Methods  
SOM Text  
Figs. S1 to S3  
References and Notes

18 August 2003; accepted 14 October 2003  
Published online 30 October 2003;  
10.1126/science.1090561  
Include this information when citing this paper.

# Nanowire Crossbar Arrays as Address Decoders for Integrated Nanosystems

Zhaohui Zhong,<sup>1\*</sup> Deli Wang,<sup>1\*</sup> Yi Cui,<sup>1</sup> Marc W. Bockrath,<sup>3</sup>  
Charles M. Lieber<sup>1,2,†</sup>

The development of strategies for addressing arrays of nanoscale devices is central to the implementation of integrated nanosystems such as biological sensor arrays and nanocomputers. We report a general approach for addressing based on molecular-level modification of crossed semiconductor nanowire field-effect transistor (cNW-FET) arrays, where selective chemical modification of cross points in the arrays enables NW inputs to turn specific FET array elements on and off. The chemically modified cNW-FET arrays function as decoder circuits, exhibit gain, and allow multiplexing and demultiplexing of information. These results provide a step toward the realization of addressable integrated nanosystems in which signals are restored at the nanoscale.

The past several decades have witnessed major advances in computing that have resulted from systematic reductions in feature sizes and the corresponding increases in integration densities achieved by the semiconductor industry (1). Recognition of possible barriers to the continuation of these trends has led to substantial work focused on exploring nanoscale device elements, including molecules (2, 3), carbon nanotubes (NTs) (4–7), and semiconductor nanowires (NWs) (8–10), and on developing methods for the creation of organized and interconnected high-density arrays of these elements (11–14). Considerable progress has been made recently in both of these areas, although integrated architectures for nanocomputing will also require schemes for addressing elements within ar-

rays at the nanoscale (15). The importance of being able to address nanoscale elements in arrays goes beyond the area of nanocomputing and will be critical to the realization of other integrated nanosystems such as chemical/biological sensors (16, 17) and

electrically driven nanophotonics (9, 18).

We report an approach to this general problem based upon a scalable crossed-nanowire field-effect transistor (cNW-FET) architecture, in which molecular-level modification of specific cross points within arrays is used to define an address code that enables NW input lines to turn on and off specific output lines. This basic array structure functions as an address decoder, with signal restoration at the nanoscale because of the inherent gain of the cNW-FET elements. The underlying issue for addressing can be understood when we consider a regular cNW-FET array (Fig. 1A) that consists of  $n$ -input ( $I_1, I_2, \dots, I_n$ ) and  $m$ -output ( $O_1, O_2, \dots, O_m$ ) NWs, in which outputs are the active channels of FETs and the inputs function as gate electrodes that turn these output lines on and off (10). When a voltage is applied to  $I_n$  in a regular array, it will affect each of the output NWs in the same way, which precludes selective addressing of elements. We overcame this critical limitation by differentiating cross points such that inputs affected only specific output cross points in the array. In the simplest scenario in which one output NW is turned on or off by a single input, differentiation of diagonal elements of a square array (Fig. 1A)

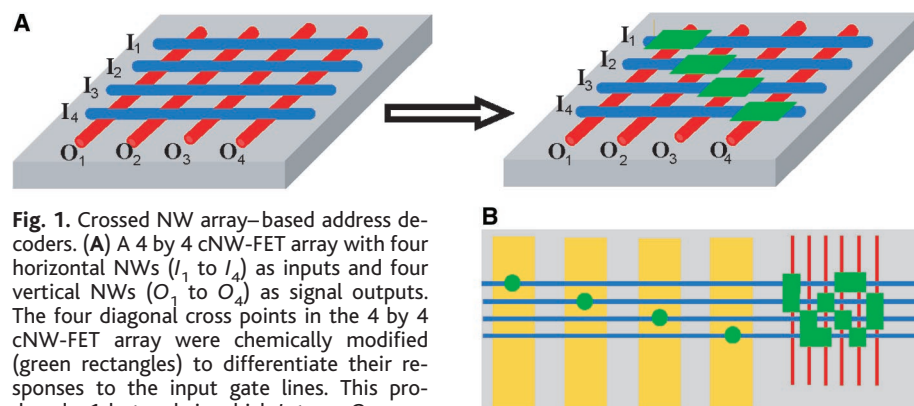


**Fig. 1.** Crossed NW array-based address decoders. **(A)** A 4 by 4 cNW-FET array with four horizontal NWs ( $I_1$  to  $I_4$ ) as inputs and four vertical NWs ( $O_1$  to  $O_4$ ) as signal outputs. The four diagonal cross points in the 4 by 4 cNW-FET array were chemically modified (green rectangles) to differentiate their responses to the input gate lines. This produced a 1-hot code in which  $I_n$  turns  $O_n$  on or off. **(B)** Bridging between microscale metal wires (yellow) and denser nanoscale NWs is achieved with a 2-hot code (green rectangles), whereby two inputs (blue NWs) are required to address each output (red NWs). The input NWs can be turned on or off by specific microscale wires with a simple 1-hot code.

<sup>1</sup>Department of Chemistry and Chemical Biology, <sup>2</sup>Division of Engineering and Applied Sciences, Harvard University, Cambridge, MA 02138, USA. <sup>3</sup>Department of Applied Physics, California Institute of Technology, Pasadena, CA 91125, USA.

\*These authors contributed equally to this work.

†To whom correspondence should be addressed. E-mail: [cml@cmliris.harvard.edu](mailto:cml@cmliris.harvard.edu)